



Interfacial ferromagnetism in reduced graphene oxide–ZnO nanocomposites

Kamarajan Thiyagarajan¹ · Munisamy Muralidharan² · Kandasamy Sivakumar¹

Received: 11 November 2017 / Accepted: 5 February 2018 / Published online: 7 February 2018
© Springer Science+Business Media, LLC, part of Springer Nature 2018

Abstract

Reduced Graphene Oxide (rGO) and rGO–ZnO nanocomposites have been successfully prepared by hydrothermal and solvothermal method, respectively. Powder XRD and Raman spectroscopy studies confirmed the formation of nanocomposites. The nanostructures of samples were imaged and found that ZnO nanoparticles covered over rGO sheets. The reduction of various oxygen containing functional groups attached on the few layered graphitic planes and the presence of oxygen vacancies in nanocomposites were confirmed by XPS. The relative contribution of PL emission bands in composites arises due to the existence of intrinsic defects. The M–H curve of rGO sheets and rGO–ZnO nanocomposites exhibit ferromagnetic behavior. The decrease of magnetization in composites owing to increases the rGO ratio leads to decrease the oxygen vacancies in the surface of ZnO nanoparticles.

1 Introduction

Materials comprising both semiconducting and magnetic features have been potential candidates for the field of spintronics [1]. In the past decade, lot of research works have been done on semiconductors holding a small amount of magnetic impurities (Fe, Co and Ni) called diluted magnetic semiconductors (DMS) [2]. The origin of ferromagnetism in DMS materials are controversial, whether the ferromagnetic ordering comes from magnetic ions at the substitution sites or arises from segregation of magnetic impurities or occurrence of secondary magnetic phases [3–5]. In particular, Zinc oxide (ZnO) is a wide band gap (3.3 eV) semiconductor with large exciton binding energy (60 meV) at room temperature, which also exhibits room temperature ferromagnetism by doping with either magnetic or non-magnetic elements [1, 5, 6]. Additionally, the existence of surface (intrinsic) defects in pure ZnO nanostructures also induces ferromagnetism. Moreover, high surface to volume ratio and intrinsic defects in ZnO nanostructures generate large number of uncompensated surface spin, which give rise to long range

ferromagnetic order [7, 8]. Hence, defects levels in the band gap of semiconductor has localized states which induces spin polarization results in ferromagnetism. Various mechanisms have been used to explain the ferromagnetism in ZnO nanostructures. In specific, grain boundary model was proposed to explain the source of ferromagnetism in ZnO thin films [9]. It is a result of strongest magnetic interaction between those isolated magnetic moments in grain boundary surface induces room temperature ferromagnetism. Further, tunable ferromagnetism was achieved in carbon doped ZnO nanostructures due to the charge transfer mediated between Zn 4s and C 2p orbitals and breaks the carbon–carbon interaction mediated by oxygen. This result confirmed that the decrease of saturation magnetization while the content of carbon atom increases in ZnO lattice. It may be ascribed to non uniform distribution of carbon that forms magnetic inactive defects [10].

Organic molecules covered over defective ZnO nanostructures have drawn considerable attention for future spintronics [11, 12]. In literature, tunable room temperature ferromagnetism was achieved by various organic molecules capped on ZnO nanoparticles [13, 14]. These results reveal that the wrapping of organic molecules may alter the electronic configuration of ZnO nanoparticles. Recently, graphene/rGO sheets are used instead of organic molecules to modify the electronic states of ZnO nanoparticles [15, 16]. Generally, graphene is a single layer of sp²-hybridized carbon atoms which are packed in hexagonal (honeycomb) structure. It is

✉ Kamarajan Thiyagarajan
thiyaguphysics@gmail.com

¹ Department of Physics, Anna University, Chennai 600 025, India

² Department of Nuclear Physics, University of Madras, Chennai 600 025, India

a two-dimensional sheet with a 0.34 nm thickness that has remarkable electrical, mechanical, thermal and high surface area properties [17]. But, pure graphene is non-magnetic due to delocalized π -bonding network which restricts its magnetic behavior, but theoretically it is predicted that the existence of defects such as topological, vacancy and zigzag edges states are exhibit ferromagnetism [18, 19]. Experimentally, graphene/rGO sheets induce ferromagnetism have been reported [20]. It is attributed to cutting of graphite crystal during oxidation process, as well as reduction of various oxygen functional groups ($-\text{OH}$, $-\text{O}-$, $-\text{COOH}$ and $\text{C}=\text{O}$) on GO, which breaking the π bond network to create localized electronic states at their grain boundaries [21]. Compared with organic shells molecules, rGO sheets have unsaturated π orbitals (p_z) and lack of band gap [22]. This is favorable for electronic interaction with 3d orbitals of transition-metal ions in oxide semiconductors. It has been recently reported that rGO–semiconducting oxide nanocomposites such as rGO–ZnO [23], rGO– SnO_2 [24] and rGO– WO_3 [25] demonstrates the tunable ferromagnetic behavior. It arises due to spin polarized electron transport occurred by interfacial charge transfer across the semiconductor nanocrystals and rGO sheets. However, there is no significant work on ZnO nanoparticles covered on various ratios of rGO sheets for the tunable room temperature ferromagnetism.

Motivation of the present work is to realize the origin of ferromagnetic nature in rGO sheets and ZnO nanoparticles separately. Discussed elaborately, the inclusion of rGO sheets influences the electronic band structure of defective ZnO nanoparticles which exhibit tunable ferromagnetism. Hence, in this study a systematic investigation of both rGO sheets and rGO–ZnO nanocomposites were carried out in order to understand the room temperature ferromagnetism.

2 Experimental section

2.1 Materials

Graphite microcrystal with particle size of 3–15 μm (99.999%), Zinc acetate dehydrate and dimethylformamide (DMF) were purchased from Alfa Aesar. NaNO_3 , KMnO_4 (Extrapure AR), H_2SO_4 (98%, GR Proanalysis), H_2O_2 (30% GR Proanalysis) and HCl (35% GR Proanalysis) were purchased from MERCK and used as received without further purification. Millipore water (H_2O) was used as solvent during experiments.

2.2 Hydrothermal reduction of GO

Graphene Oxide (GO) was obtained from microcrystalline graphite by modified Hummer's method [24]. In a typical procedure, one of the ratios of GO powder (160 or 320 mg)

was dispersed in 160 ml of Millipore water and ultrasonicated for 1 h. After, highly dispersed GO solution was transferred into 200 ml of Teflon coated stainless steel autoclave and kept at 180 °C for 8 h. The obtained product was washed using vacuum filtration with ethanol and dried at 60 °C for 5 h in vacuum oven. Hydrothermally reduced 160 mg of GO dispersed (1 mg/1 ml) product was named as 1HrGO and 320 mg of GO dispersed (2 mg/1 ml) product was named as 2HrGO.

2.3 Preparation of rGO–ZnO nanocomposites

In a typical procedure, 40 mg of GO was uniformly dispersed in 40 ml of DMF by ultrasonication for 30 min. About 0.92 g of Zinc acetate dehydrate [$\text{Zn}(\text{CH}_3\text{COO})_2 \cdot 2\text{H}_2\text{O}$] was dissolved in 200 ml of DMF, subsequently GO solution was added into the above solution and continually stirred until the formation of a stable precursor. The mixed solution was heated at 95 °C and maintained at that temperature for 5 h. The color of mixture was changed from white to grey. After aging, the product was extracted from column chromatography using silica gel and washed with ethanol by centrifugation. The final product was obtained after drying in vacuum at 55 °C and labeled as SrGO–ZnO nanocomposite. Above procedure was followed for 1HrGO and 2HrGO samples in DMF and were labeled as 1HrGO–ZnO and 2HrGO–ZnO nanocomposites, respectively. Pure ZnO was prepared by the same procedure without adding GO.

2.4 Characterization techniques

The Powder X-ray diffraction of all the samples were carried out by Bruker D2 PHASER X-Ray Diffractometer using $\text{CuK}\alpha$ (1.5418 Å) radiation in the 2θ range of 10°–80°. Raman spectra were recorded using LabRAM HR (Horiba-Jobin) with the excitation wavelength of 514 nm by Argon-ion laser. The crystal structure and morphology of the nanocomposites were examined using high-resolution transmission electron microscopy (HRTEM, JEOL JEM-2010, Japan). X-ray photoelectron spectroscopy (XPS) spectra were recorded using KRATOS analytical equipment with $\text{AlK}\alpha$ radiation ($h\nu = 1486.6$ eV). The photoluminescence (PL) spectra were recorded using Perkin-Elmer spectrophotometer with an excitation wavelength of 385 nm. The magnetic behaviors of the samples were analyzed using Lake-shore vibrating sample magnetometer (VSM-7410).

3 Results and discussion

3.1 XRD analysis

Figure 1 shows the XRD patterns of Graphite, GO, 1HrGO and 2HrGO samples. The diffraction peak of pure graphite

appears at 26.5° (2θ) corresponding to the interlayer spacing of $d_{002} = 0.335$ nm and consisted with the (002) peak of graphitic systems. After the oxidation of graphite in the strong acid medium as GO, a diffraction peak appeared at 11.28° (2θ) and the interlayer distance increased from 0.335 nm (graphite) to 0.79 nm (GO). During the oxidation process of graphite, various oxygen containing functionalities like hydroxyl, epoxy, carbonyl and carboxyl groups attached on the basal plane and edges of GO sheets. After hydrothermal reduction of GO, (002) planes of GO sheets are shift to higher angle (2θ) around 25° as rGO sheets. The calculated interlayer distances of 1HrGO and 2HrGO sample are 0.38 and 0.36 nm respectively. These values are much lower than that of GO precursor (0.79 nm) at the same time a little higher than that of natural graphite (0.335 nm). These results suggest that the presence of residual oxygenated functional groups which present in GO sheets were removed and the layers got formed. The broad XRD peak of both 1HrGO and 2HrGO also indicates the poor ordering of graphene network along their stacking direction to form the framework of few-layer stacked graphene sheets [26]. Further, XRD patterns of pure ZnO and rGO–ZnO nanocomposites are shown in Fig. 2. The diffracted peaks of pure ZnO at 2θ values of 31.9, 34.5, 36.4, 47.6, 56.7 and 63 are assigned to (100), (002), (101), (102), (110) and (103) planes, which are consistent

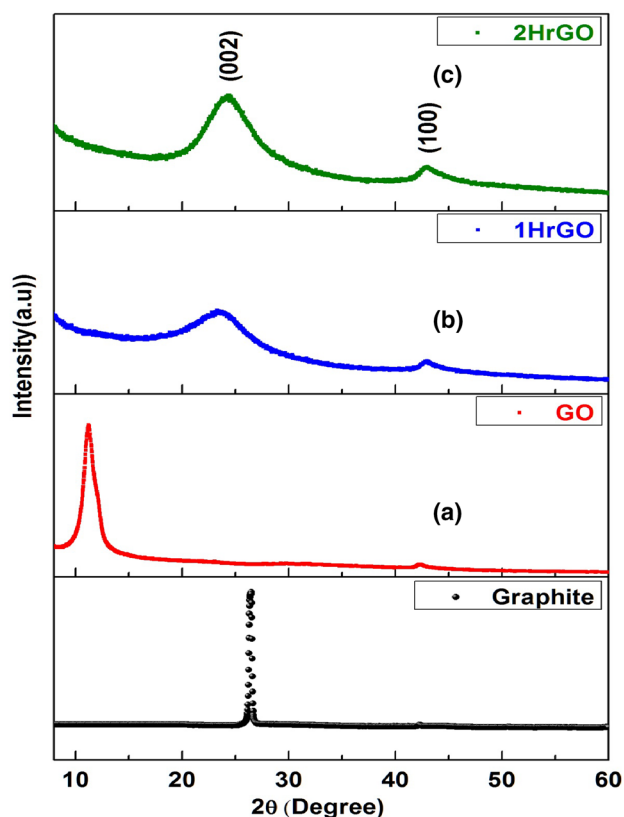


Fig. 1 Powder XRD pattern of (a) GO, (b) 1HrGO and (c) 2HrGO

with the standard JCPDS data [PDF no. 36-1451] and confirmed the wurtzite structure of hexagonal ZnO. All diffraction patterns of nanocomposites (SrGO–ZnO, 1HrGO–ZnO and 2HrGO–ZnO) are consistent with the wurtzite structure of ZnO; since the presence of rGO sheets does not affect the diffraction peaks of ZnO. The characteristic diffraction peaks of rGO is not observed in composites, which is due to the self-reassembling of exfoliation of layered GO as well as low amount and relatively weak intensity of rGO sheets compared with ZnO. The crystallite average size of pure ZnO was 8 nm as measured by Scherrer formula; meanwhile ZnO on rGO sheets had same crystallite average size of 8 nm. Hence, the incorporation of rGO sheets does not affect the size of ZnO crystallites [27].

3.2 Raman analysis

Raman spectroscopy is effective tool to identify the order–disorder parameters of carbon nanostructures. The typical Raman spectra of GO, 1HrGO and 2HrGO are shown in Fig. 3 (top). Two distinct peaks of GO appeared at 1356 and 1592 cm^{-1} are assigned to D and G band of graphite. The graphitic layer of G band is ascribed to the first-order scattering of E_{2g} symmetry and the D band corresponds to defects/disorder of graphitic structure with the k-point phonons of A_{1g} symmetry. The intensity ratio (I_D/I_G) of sample is frequently used to estimate the structural changes during the oxidation and reduction of GO sheets. After hydrothermal process of GO, the G band of 1HrGO and 2HrGO samples peaks were shift to lower wavenumber, which indicates the reduction of GO. The calculated intensity ratio (I_D/I_G) of GO, 1HrGO and 2HrGO are 1.1, 0.97 and 0.92 respectively. The decrease of intensity ratio

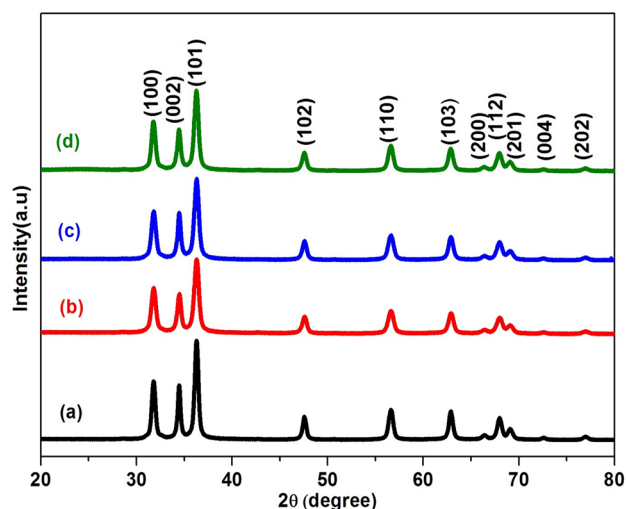


Fig. 2 Powder XRD pattern of (a) pure ZnO, (b) SrGO–ZnO, (c) 1HrGO–ZnO and (d) 2HrGO–ZnO nanocomposites

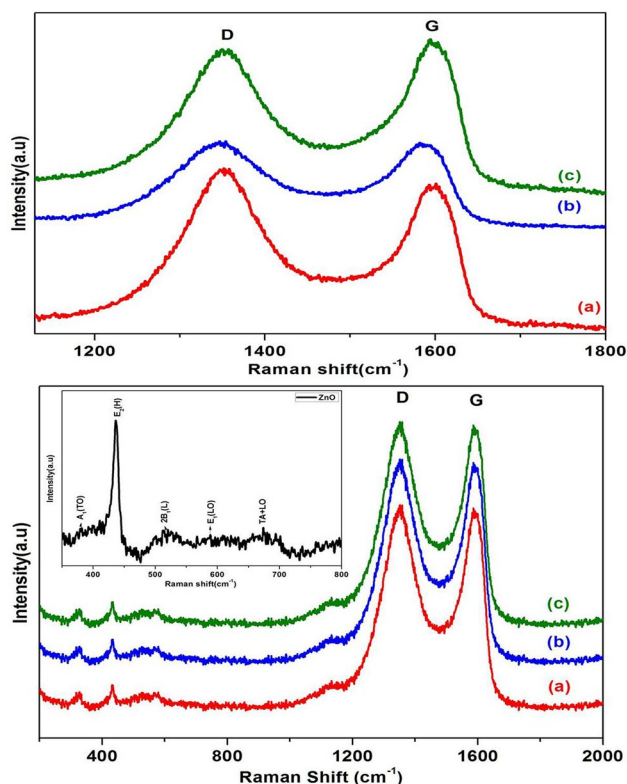


Fig. 3 Raman spectra of (a) GO, (b) 1HrGO and (c) 2HrGO (top), Raman spectra of (a) pure ZnO, (b) SrGO–ZnO and (c) 1HrGO–ZnO, (d) 2HrGO–ZnO nanocomposites (bottom)

(I_D/I_G) in rGO samples (1HrGO and 2HrGO) compared with GO due to the restored more fragmentation of sp^2 domain by defect repairing mechanism [28]. Moreover, the various intensity ratios (I_D/I_G) of these samples are associated to structural distortion and surface rippling, which are occurred in the graphene lattice by the restoration of carbon sp^2 bonds and de-oxidation under reduction [29]. Since, it is clearly observed that the formation of defects in graphitic layer during the oxidation and removal of various functional groups attached on the plane of rGO sheets which induces disorder. The strong D band in rGO samples may be favorable for the occurrence of ferromagnetism. Further, Raman spectra of ZnO, rGO–ZnO nanocomposite are depicted in Fig. 3(bottom). Insert Fig. 3(bottom) shows pure ZnO in which there are five vibration peaks at 377, 435, 537, 581 and 664 cm^{-1} , which correspond to vibration mode of $A_1(TO)$, $E_2(H)$, $2B_1(L)$, $E_1(LO)$ and $TA+LO$. Among these, the highest intensity of $E_2(H)$ mode confirmed the wurtzite structure of ZnO. The $E_1(LO)$ and $2B_1(L)$ mode arise owing to induced surface defect such as oxygen vacancies on the surface of ZnO nanoparticles [7]. Further, carbon and ZnO vibrations are observed in rGO–ZnO nanocomposites. These results are indicated that ZnO covered over rGO sheets and confirmed the vibration modes of ZnO and

rGO sheets [30]. The calculated intensity ratio (I_D/I_G) of rGO sheets in SrGO–ZnO, 1HrGO–ZnO and 2HrGO–ZnO nanocomposites are 0.99, 0.95 and 0.90 respectively. These results also reveal that the interaction between rGO sheets and ZnO particles during solvothermal process.

3.3 HRTEM analysis

The bright-field HRTEM images of ZnO and rGO–ZnO composites are shown in Fig. 4. The enlarged sight of the HRTEM image of ZnO nanoparticles with average particle size of 8 nm illustrate in Fig. 4a. The interplanar spacing of ZnO is 0.26 nm as observed in Fig. 4b, which is matched with previous XRD (002) planes of ZnO. The Selected Area Electron Diffraction (SAED) patterns of ZnO nanoparticles have shown the ring patterns which matched to crystallographic Bragg's planes and indexed, confirms wurtzite structure as shown in Fig. 4c. ZnO nanoparticles covered on the surface of rGO sheets and corresponding to SAED pattern shows the existence of rGO and ZnO planes are denoted in Fig. 4d, f. It is clearly seen that rGO sheets does not affect the crystalline structure and size of ZnO nanoparticles [31]. The ZnO nanoparticles coated over hydrothermally reduced GO samples (1HrGO and 2HrGO) are seen in Fig. 4g, j, corresponding to SAED pattern in Fig. 4i, l. It is possible that ZnO nanoparticles decorated over the different aspect ratio of rGO sheets and ensure that the size and shape of ZnO nanoparticles remains unchanged, only systematic influence of different rGO ratio. It is also observed that the incorporation of rGO sheets does not deteriorate/alter the preferential orientation and crystallinity of ZnO surface [31].

3.4 XPS analysis

XPS is an important tool for detection of chemical composition, oxidation state and defect nature on the surface of samples. The survey spectra of GO and 2HrGO samples are shown in Fig. 5a, b, only two peaks appeared around 284.5 and 531.3 eV are indexed to C 1s and O 1s which confirm the chemical composition of carbon and oxygen. From these survey spectra, the peak intensities of O 1s of 2HrGO sample are greatly weak compared with O 1s of GO. This result clearly indicates that the decreases of oxygen functional groups in 2HrGO replicate the formation of layered graphene network. In Fig. 5c depict C 1s peak of GO was deconvoluted into two broad peaks at 285.3 and 287.8 eV, which are related to sp^3 C–C and C=O (carbonyl) respectively. The resultant of sp^3 C–C occurred due to broken of sigma carbon bonds during the oxidation of micro-sized graphite have large amount of oxygen functional groups attached on the surface. In Fig. 5d, the C 1s spectra of 2HrGO were deconvoluted into three peaks at 284.5, 285.7 and 288.6 eV which are assigned to sp^2 C–C,

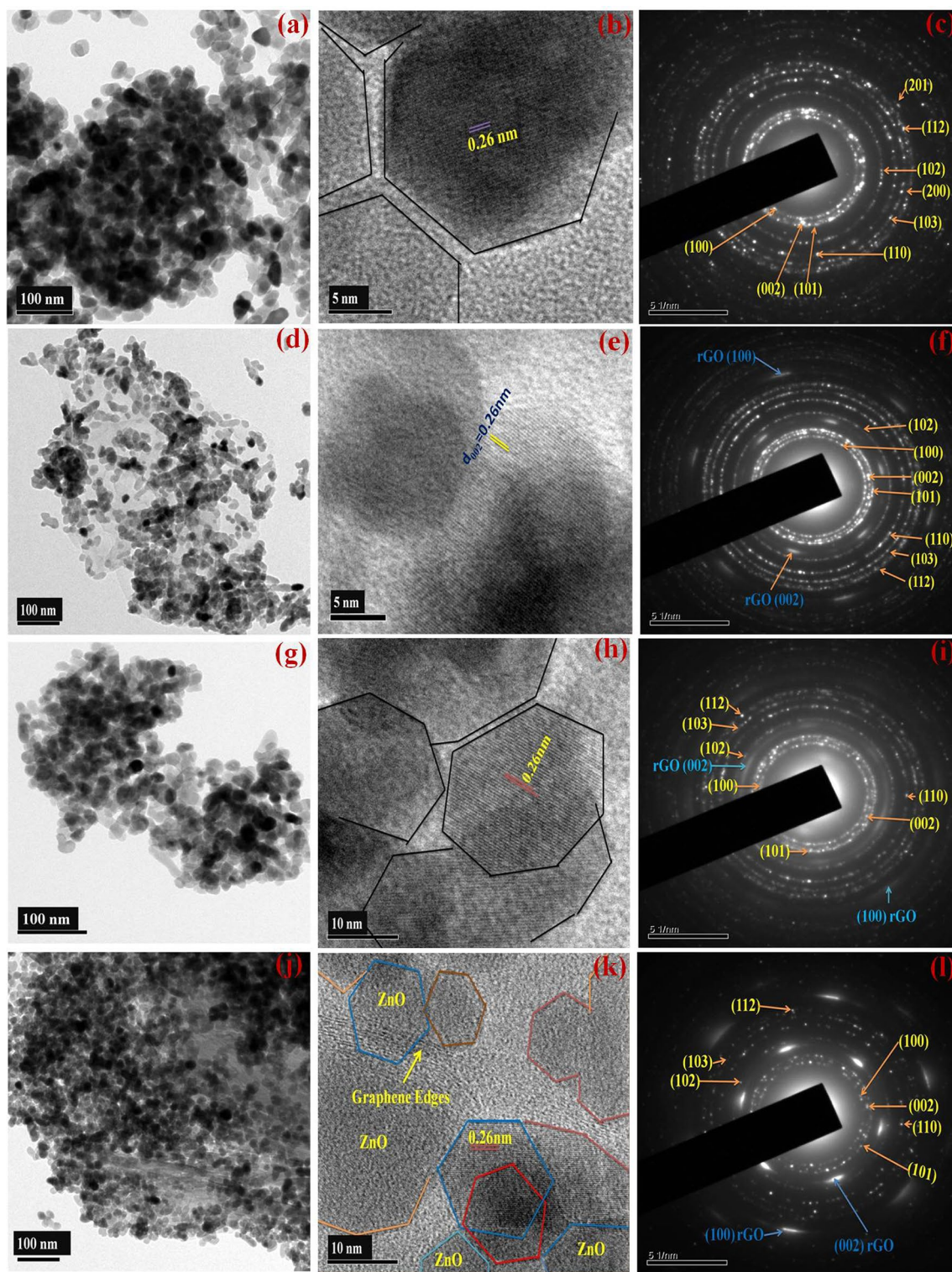


Fig. 4 HRTEM image of **a** ZnO, **d** SrGO–ZnO, **g** 1HrGO–ZnO and **j** 2HrGO–ZnO nanocomposite and corresponding lattice fringe pattern (**b**, **e**, **h**, **k**), as well as SAED pattern of **c** ZnO, **f** SrGO–ZnO, **i** 1HrGO–ZnO and **l** 2HrGO–ZnO

sp^3 C–C and O–C=O (carboxyl) respectively. It is observed that most of the sp^3 C–C restored into sp^2 C–C during hydrothermal methods, but small amount of sp^3 C–C exist

in 2HrGO samples. Further, to understand the typical O 1s spectra of GO and 2HrGO are depicted in Fig. 5e, f. The O 1s spectra of GO were deconvoluted into two main peaks

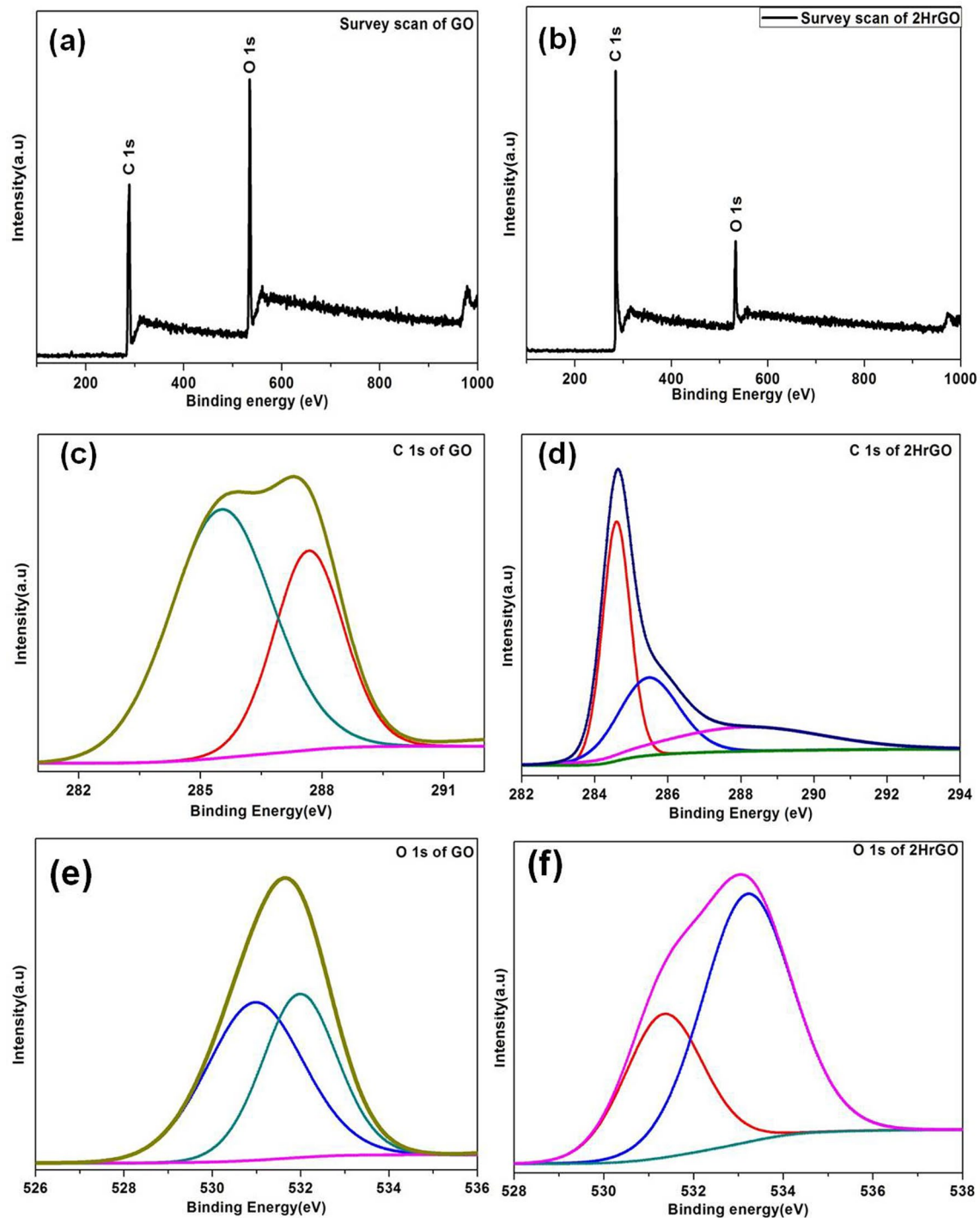


Fig. 5 XPS spectra of **a** survey scan of GO, **b** survey scan of 2HrGO, **c** C 1s of GO, **d** C 1s of 2HrGO, **e** O 1s of GO and **f** O 1s of 2HrGO

at 531.1 and 533.3 eV which are related to hydroxyl, carboxyl groups. Since, carboxyl groups typically located at sheet edges and the OH groups is covalently bond to the basal-plane of carbon atoms to form sp^3 -type defects. The O 1s spectra of 2HrGO were deconvoluted into two main groups at 530 and 532.6 eV are corresponding to C–O and

C–O–C (epoxy groups). Hence, the restored from sp^3 to sp^2 carbon during reduction of GO, which create vacancies and topological defects with unpaired electron spins contribute the ferromagnetism [32].

The XPS survey spectra of ZnO and 2HrGO–ZnO nanocomposite are shown in Fig. 6a. It is revealed that the

indexed peaks correspond to oxygen, carbon, and zinc. The double spectral lines of Zn 2p at the binding energy of 1022.7 eV (Zn 2p_{3/2}) and 1045.7 eV (Zn 2p_{1/2}) with a spin–orbit splitting of 23 eV, which confirm the zinc is present as Zn²⁺, as seen in Fig. 6b. The peak position of Zn 2p in 2HrGO–ZnO sample were slightly moved to higher

energy by anion exchange, which suggested that the fluctuation in the interfacial zinc-carbon bonding states leads to increase spin–orbit splitting 23.2 eV, as Fig. 6b. Hence, the presence of rGO sheets is not affected the chemical state of Zn²⁺ in composites [33]. Asymmetric peak of O 1s of ZnO sample was deconvoluted into two peaks by fitting of

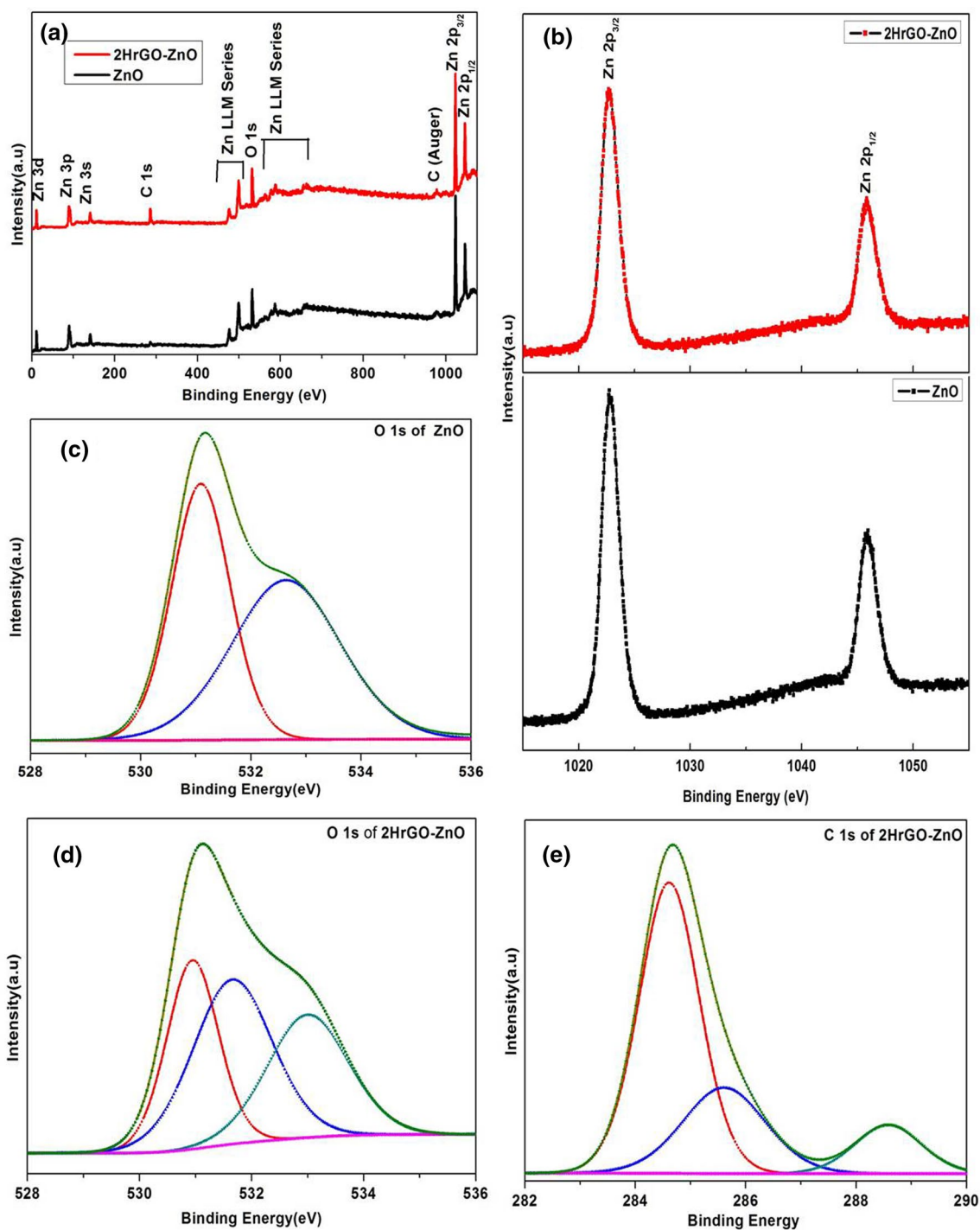


Fig. 6 XPS spectra of **a** survey scan of ZnO and 2HrGO–ZnO nanocomposite, **b** Zn 2p of ZnO and 2HrGO–ZnO, **c** O 1s of ZnO, **d** O 1s of 2HrGO–ZnO, and **e** C 1s of 2HrGO–ZnO

Gaussian distribution as depicted in Fig. 6d. The main peak is located at 531.1 eV assigned to the O^{2-} ion in the wurtzite structure bounded by the zinc ions with their full balance of nearest-neighbor O^{2-} ions. The peak at 533 eV is attributed to loosely bound oxygen, adsorbed O_2 or adsorbed H_2O on the ZnO surface [34]. From the Fig. 6e, O 1s core-level peak of 2HrGO–ZnO spectra can also be resolved into three components centered at 530.9, 531.8, and 533.4 eV by a Gaussian function with a slightly lower energy as compared to ZnO. The carbon is bonded at oxygen site in ZnO, hybridization and delocalized 2p of carbon and 4s of Zn orbital's to create charge transfer in composites. These interpretations believe that the support of ZnO nanoparticles is acutely covered over rGO sheets and allow minimum oxygen contribution on the surface of ZnO nanoparticles. Figure 6c, the C 1s spectrum of 2HrGO–ZnO sample is deconvoluted into two different peaks centered at 284.4 and 288.6 eV corresponding to C–C, O–C=O (carboxyl groups) respectively [21]. It is clearly seen that the absence of hydroxyl, epoxy and carbonyl functional groups on the rGO sheets, only restored sp^2 (C–C) and small amount of carboxyl (O–C=O) groups on rGO sheets in 2HrGO–ZnO samples.

3.5 PL analysis

PL studies reveal that the presence of intrinsic defects in pure ZnO nanoparticles and rGO–ZnO nanocomposite as depicted in Fig. 7. All the samples exhibit visible band emission in the range 400–550 nm, which indicates that several kinds of intrinsic defects and vacancies are present in these samples. In literature, these kinds of emission are originated from zinc interstitial, zinc vacancies, oxygen vacancies having different charged state and oxygen interstitials in ZnO nanostructures, which occur near the blue-green-yellow emission [35]. The band-to-band emission peak of all samples could not be observed in the present investigation due

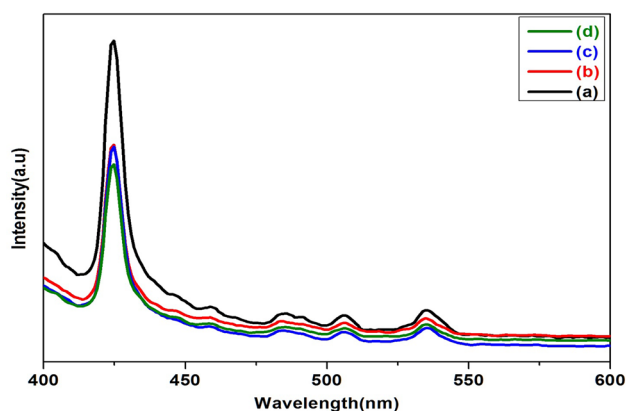


Fig. 7 PL spectra of (a) ZnO, (b) SrGO–ZnO, (c) 1HrGO–ZnO and (d) 2HrGO–ZnO nanocomposites

to limitation of PL detection range. A high intense emission peak of ZnO at 425 nm is assigned to Zinc interstitial level (Zn_i). The high intensity of this peak shows high formation energy of Zinc interstitial (Zn_i) due to the large number of nanograin boundaries [7]. The blue emission peak at 462 nm originates from neutral oxygen vacancies. The green emission band at 506 nm is assigned to zinc vacancy (V_{zn}) and 534 nm is attributed to singly charged oxygen vacancy which acts as an electron trap on the surface of ZnO. The presence of V_{zn} and V_o put together leads to green light emission. The formation energy of oxygen vacancies is lower than Zinc vacancies and Zinc interstitial in the surface of ZnO nanoparticles [36, 37]. Similarly, rGO–ZnO nanocomposites show same emission peaks, but the intensity of peaks are decreased compared to pure ZnO. Hence, the presence of rGO sheets leads to decrease the intrinsic defect density on the surface of ZnO nanoparticles.

3.6 Magnetic studies

The magnetization versus field (M – H) dependent curves of GO and rGO sheets are measured at room temperature with applied field range of $-15 \text{ kOe} < H < 15 \text{ kOe}$ as depicted in Fig. 8. It has been observed that GO is weak ferromagnetic with dominant diamagnetic signals. Saturated magnetization (M_s) of GO is 0.003 emu/g, it matches with earlier reported value [38]. Generally, GO is composed of an unreacted graphite (sp^2) region and a reacted (sp^3) region with partially distorted layers. There are randomly distributed like epoxy and hydroxyl, carbonyl and carboxyl functional groups on each plane in the reacted region of GO. Carboxyl and carbonyl groups are normally located at the edge sites of GO sheets, whereas hydroxyl and epoxy groups are adsorbed on the basal plane of GO sheets [39–41]. It is energetically favorable to place the epoxy groups on the opposite side

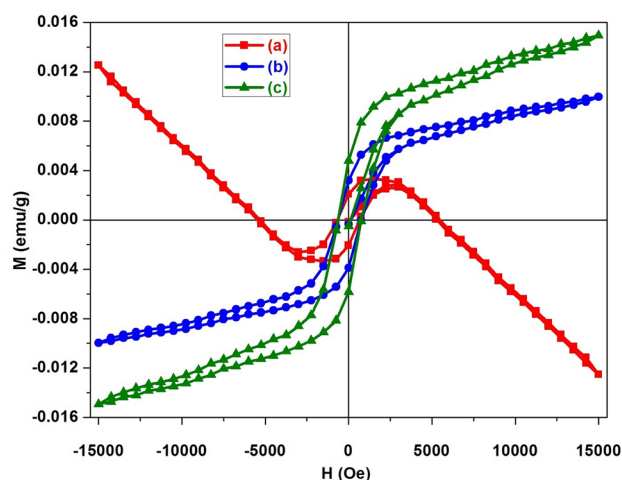


Fig. 8 M – H curve of (a) GO, (b) 1HrGO and (c) 2HrGO

of hexagonal ring induce magnetic moment [42]. Moreover, graphitic edge state is magnetically active due to the presence of non-bonding with a large local density of states which act as localized spin and the vacancies with dangling bonds also have spin units. In addition, edge states are populated with unpaired electron spin to minimize the coulomb repulsive energy, leads to large moments at the zigzag edge boundary. At the same time, high concentration of sp^3 type defects (OH) is remained on the basal plane of GO sheets, which are effectively induced magnetic moments [42, 43]. The saturation magnetization (M_s), remanent magnetization (M_r) and coercivity (H_c) values of GO and rGO sheets are listed in Table 1. In our work, weak ferromagnetism arises in GO by interaction between separated magnetic regions and domains. The negative slop of GO at high field indicates strong diamagnetic contribution, which is generated by the attachment of carbonyl and hydroxyl groups located at edge site and on the basal plane of GO, respectively. After hydrothermal reduction of GO sheets, increase in the number of zigzag edges in 1HrGO sample had strong ferromagnetism. Removal of functional groups cause defects in the form of vacancies, structural defects and distortion in the lattice of GO which leads to ferromagnetic behaviour. Meanwhile, some of the damaged sp^2 carbon conjugations are restored and generated partial coalescing of rGO sheets which significantly increases the amount of π - π staking sites. So, the existence of high density of defects, which arise net spin moment in rGO sheets. Moreover, the removal of carbonyl groups can compensate the dangling bond and preserve the edge states magnetism [19]. Finally, 2HrGO sample had high saturation magnetization of 0.015 emu/g and coercivity of 563 Oe which is higher value comparable to previously reported value of rGO sheets [44]. Since reduced wrinkles contain two important effects, which is average local magnetic anisotropy energy density and coming out of longer range magnetic interaction/ordering [45]. The long range ordering (magnetically coupling) of these spin exists due to a tiny crystalline size and a large quantity of grain boundaries among small portions of rGO sheets, which is contribute to the ferromagnetism.

At room temperature M–H loops of ZnO and rGO–ZnO nanocomposites are depicted in Fig. 9. The hysteresis loop of ZnO nanoparticles clearly exhibit room temperature

ferromagnetism. The saturation magnetization (M_s), remanent magnetization (M_r) and coercivity (H_c) values of ZnO nanoparticles and rGO–ZnO nanocomposites are given in Table 2. Experimentally, the origin of ferromagnetism in pure ZnO nanostructures should be associated with various kinds of structural defects (oxygen vacancies, zinc vacancies, zinc interstitials and oxygen interstitials) present in the lattice sites; these point defects induce magnetic moments [46, 47]. Since the population of defects in ZnO particles is usually not large and uniform, the magnetization value of these specimens is very small compared to magnetic oxides [48]. The high surface to volume ratio of ZnO nanoparticles have higher density of oxygen vacancies and create surface spin disorder. The intrinsic defects nature of ZnO was previously confirmed by PL spectra. At the same time, our XPS and Raman results confirmed that the oxygen vacancies present in ZnO samples. From these observations, uncontrolled formation of lattice defects during preparation may form the ferromagnetic domains. It is proposed that F-centre exchange mechanism explain the interaction between isolated spin magnetic moments in lattice site of ZnO nanoparticles [49]. Experimentally

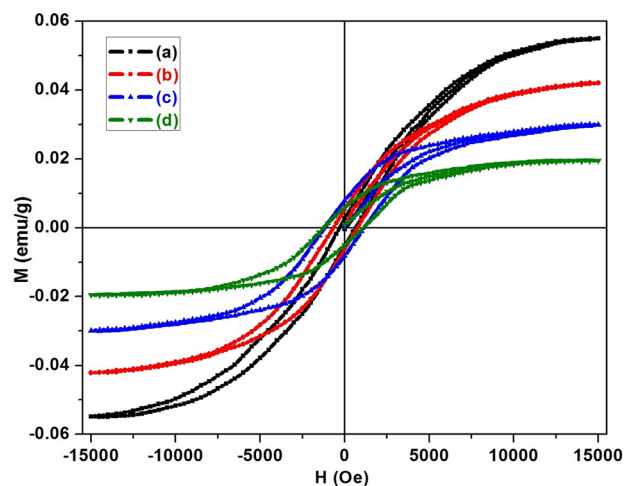


Fig. 9 M–H curve of (a) ZnO, (b) SrGO–ZnO, (c) 1HrGO–ZnO and (d) 2HrGO–ZnO nanocomposites

Table 1 Magnetization values of GO and rGO Sheets

Sample	Saturation magnetization (M_s) in memu/g	Remanent Magnetization (M_r) in memu/g	Coercivity (H_{ci}) Oe
GO	3.53	2.08	358
1HrGO	9.05	3.51	439
2HrGO	15.05	5.2	563

Table 2 Magnetization values of ZnO and rGO–ZnO nanocomposites

S. No.	Saturation magnetization (M_s) in memu/g	Remanent Magnetization (M_r) in memu/g	Coercivity (H_{ci}) Oe
ZnO	55.4	2.54	321
SrGO–ZnO	40.6	5.38	476
1HrGO–ZnO	28.9	7.76	768
2HrGO–ZnO	19.9	6.52	893

achieved and reported the highest value M_s and H_c of pure ZnO nanostructures are 6.1emu/g and 360 Oe [50].

Further, the hysteresis loop of rGO–ZnO nanocomposites clearly shows room temperature ferromagnetism. The saturation magnetization of rGO–ZnO nanocomposites decreases compared with pure ZnO nanoparticles. It is attributed to the non-uniform distribution of rGO sheets form magnetically inactive defects and increase in the shell layers of rGO sheets covered ZnO core induces a weak interaction. These thick shell layers of rGO sheets making C atoms, which leads to crosslink each other within the shell rather than ZnO core. It may be wrapping of rGO sheets reduces the oxygen vacancy concentration on the surface of ZnO [23, 24]. The interparticle interaction of ZnO nanoparticles also decreases in nanocomposites when the rGO layer covered over ZnO nanoparticles leads to lack of long range magnetic interaction [51, 52].

4 Conclusion

A series of rGO sheets and rGO–ZnO nanocomposites were fabricated by hydrothermal method and solvothermal route, respectively. The structural and magnetic properties of samples have been investigated. The XRD analysis confirms the formation of nanocomposites and wurtzite structure of ZnO nanoparticles. Raman spectra also provide the evidence for the construction of nanocomposites. HRTEM images clearly seen that the ZnO nanoparticles attached over rGO layered sheets and SAED pattern reveal that the co-existence of both ZnO and rGO planes indexed. Chemical composition, oxidization state of the elements were identified which confirms the presence of oxygen vacancy in the prepared samples. The multi-color emission clearly shows the presence of defects and oxygen vacancy in the sample. The magnetic studies demonstrate the nanocomposites exhibits room temperature ferromagnetism. This may be attributed to defects, vacancy and interfacial effects in rGO and rGO–ZnO composites. Hence, it is concluded that the level of surface carbon atom in rGO layered adsorption by ZnO nanoparticles must also be taken into account for the tunable ferromagnetic behavior in nanocomposites.

Acknowledgements Authors acknowledged to Sophisticated Analytical Instrumentation Facility (SAIF), Indian Institute of Technology (IITM), Madras for this support on characterization of samples.

Compliance with ethical standards

Conflict of interest The authors declare that they have no conflict of interest.

References

1. M.A. Garcia, J.M. Merino, E. Fernandez Pinel, A. Quesada, J. de la Venta, M.L. Ruz Gonzalez, G.R. Castro, P. Crespo, J. Llopis, J.M. Gonzalez-Calbet, A. Hernando, Magnetic properties of ZnO nanoparticles. *Nano Lett.* **7**, 1489–1494 (2007)
2. T. Dietl, Dilute magnetic semiconductors: functional ferromagnets. *Nature Mater.* **2**, 646–648 (2003)
3. T. Kataoka, M. Kobayashi, Y. Sakamoto, G.S. Song, A. Fujimori, F.-H. Chang, H.-J. Lin, D.J. Huang, C.T. Chen, T. Ohkochi, Y. Takeda, T. Okane, Y. Saitoh, H. Yamagami, A. Tanaka, S.K. Mandal, T.K. Nath, D. Karmakar, I. Dasgupta, Electronic structure and magnetism of the diluted magnetic semiconductor Fe-doped ZnO nanoparticles. *J. Appl. Phys.* **107**, 033718 (2010)
4. H. Gu, W. Zhang, Y. Xu, M. Yan, Effect of oxygen deficiency on room temperature ferromagnetism in Co doped ZnO. *Appl. Phys. Lett.* **100**, 202401 (2012)
5. G. Srinet, R. Kumar, V. Sajal, Structural, optical, vibrational, and magnetic properties of sol-gel derived Ni doped ZnO nanoparticles. *J. Appl. Phys.* **114**, 033912 (2013)
6. S.U. Awan, S.K. Hasanain, M.F. Bertino, G.H. Jaffari, Ferromagnetism in Li doped ZnO nanoparticles: the role of interstitial Li. *J. Appl. Phys.* **112**, 103924 (2012)
7. T.-L. Phan, Y.D. Zhang, D.S. Yang, N.X. Nghia, T.D. Thanh, S.C. Yu, Defect-induced ferromagnetism in ZnO nanoparticles prepared by mechanical milling. *Appl. Phys. Lett.* **102**, 072408 (2013)
8. X. Xu, C. Xu, J. Dai, J. Hu, F. Li, S. Zhang, Size dependence of defect-induced room temperature ferromagnetism in undoped ZnO nanoparticles. *J. Phys. Chem. C* **116**, 8813–8818 (2012)
9. B.B. Stramual, S.G. Protasova, A.A. Mazilkin, G. Schutz, E. Goering, B. Baretzky, P.B. Straumal, Ferromagnetism of zinc oxide nanograined films. *JETP Lett.* **97**, 6 (2013)
10. P. Kumar, H.K. Malik, K. Asokan, Tuning of optical band gap and magnetization of C- implanted ZnO thin films. *EPL* **110**, 67006 (2015)
11. S. Deng, H. Fan, M. Wang, M.M. Zheng, J. Yi, R. Wu, H. Tan, C. Sow, J. Ding, Y. Feng, K. Loh, Thiol-Capped ZnO nanowires/nanotube arrays with tunable ferromagnetic properties at room temperature. *ACS Nano*. **4**, 495–505 (2010)
12. Y.-C. Chen, Z. Wang, A. Leineweber, J. Baier, T. Tietze, F. Philipp, G. Schutz, E. Goering, Effect of surface configurations on the room-temperature magnetism of pure ZnO. *J. Mater. Chem. C* **4**, 4166 (2016)
13. J. Chaboy, R. Boada, C. Piquer, M.A. Laguna-Marco, M. García-Hernández, N. Carmona, J. Llopis, M.L. Ruíz-González, J. González-Calbet, J.F. Fernández, M.A. García, Evidence of intrinsic magnetism in capped ZnO nanoparticles. *Phys. Rev. B* **82**, 064411 (2010)
14. G. Jayalakshmi, N. Gopalakrishnan, T. Balasubramanian, Activation of room temperature ferromagnetism in ZnO films by surface functionalization with thiol and amine. *J. Alloy. Compd.* **551**, 667–671 (2013)
15. Z. Xiang, J. Qian, Y. Zhou, F. Liu, C. Qi, X. Shi, G. Wang, S. Ye, Synthesis of quasi-core-shell Co-doped ZnO/graphene nanoparticles. *Mater. Lett.* **161**, 286–288 (2015)
16. N. Tu, N.H. Dung, N.T. Lan, K.T. Nguyen, N.D. Dung, D.X. Viet, N.T. Tuan, H.V. Bui, D.V. Nam, P.T. Huy, N. Saito, Enhanced ferromagnetism in graphite-like carbon layer-coated ZnO crystals. *J. Alloy. Compd.* **695**, 233–237 (2017)
17. F. Akbar, M. Kolahdouz, Sh Larimian, B. Radfar, H.H. Radamson, Graphene synthesis, characterization and its applications in nanophotonics, nanoelectronics and nanosensing. *J. Mater. Sci.* **26**, 4347–4379 (2015)

18. H.A.M. Vozmediano, L.P.M. Sancho, T. Stauber, F. Guinea, Local defects and ferromagnetism in graphene layers. *Phys. Rev. B* **72**, 155121 (2005)
19. R.L. Radovic, B. Bockrath, On the chemical nature of graphene edges: Origin of stability and potential for magnetism in carbon materials. *J. Am. Chem. Soc.* **127**, 5917–5927 (2005)
20. Y. Wang, Y. Huang et al., Room-temperature ferromagnetism of graphene. *Nano Lett.* **9**, 220–224 (2009)
21. S. Qin, P. Sun, Q. Di, S. Zhou, C. Yang, Q. Xu, Ferromagnetism of three-dimensional graphene framework. *RSC Adv.* **5**, 92899–92904 (2015)
22. Z. Sun, X. Yang, C. Wang, T. Yao, L. Cai, W. Yan, Y. Jiang, F. Hu, J. He, Z. Pan, Q. Liu, S. Wei, Graphene activating room-temperature ferromagnetic exchange in cobalt-doped ZnO dilute magnetic semiconductor quantum dots. *ACS Nano*. **8**, 10589–10596 (2014)
23. A. Prakash, S.K. Misra, D. Bahadur, The role of reduced graphene oxide capping on defect induced ferromagnetism of ZnO nanorods. *Nanotechnology*. **24**, 095705 (2013)
24. K. Thiyagarajan, K. Sivakumar, Oxygen vacancy-induced room temperature ferromagnetism in graphene–SnO₂ nanocomposites. *J. Mater. Sci.* **52**, 8084–8096 (2017)
25. K. Thiyagarajan, M. Muralidharan, K. Sivakumar, Defects-induced magnetism in WO₃ and reduced graphene oxide-WO₃ nanocomposites. *J. Supercond. Nov. Magn.* **31**, 117–125 (2018)
26. G. Khurana, N. Kumar, R.K. Kotnala, T. Nautiyal, R.S. Katiyar, Temperature tuned defect induced magnetism in reduced graphene oxide. *Nanoscale* **5**, 3346–3351 (2013)
27. Y. Bu, Z. Chen, W. Li, B. Hou, Highly efficient photocatalytic performance of Graphene—ZnO quasi-shell—core composite material., *ACS Appl. Mater. Interfaces* **5**, 12361–12368 (2013)
28. Y. Zhou, Q. Bao, L.A.L. Tang, Y. Zhong, P.K. Loh, Hydrothermal dehydration for the “Green” reduction of exfoliated graphene oxide to graphene and demonstration of tunable optical limiting properties. *Chem. Mater.* **21**, 2950–2956 (2009)
29. S. Qin, X. Guo, Y. Cao, Z. Ni, Q. Xu, Strong ferromagnetism of reduced graphene oxide. *Carbon*. **78**, 559–565 (2014)
30. T.N. Reddy, J. Manna, R.K. Rana, Polyamine-mediated interfacial assembly of rGO-ZnO nanostructures: a bio-inspired approach and enhanced photocatalytic properties. *ACS Appl. Mater. Interfaces*. **7**, 19684–19690 (2015)
31. D.I. Son, B.W. Kwon, D.H. Park, W.-S. Seo, Y. Yi, B. Angadi, C.-L. Lee, W.K. Choi, Emissive ZnO–graphene quantum dots for white-light-emitting diodes. *Nat. Nanotechnol.* **7**, 465–471 (2012)
32. A. Prakash, D. Bahadur, The role of ionic electrolytes on capacitive performance of ZnO-reduced graphene oxide nanohybrids with thermally tunable morphologies. *ACS Appl. Mater. Interfaces* **6**, 1394–1405 (2014)
33. Z. Gao, J. Zhang, Y. Fu, J. Xu, D. Qi, Xue, Room temperature ferromagnetism of pure ZnO nanoparticles. *Appl. Phys. Lett.* **105**, 113928 (2009)
34. X. Pan, M.-Q. Yang, Y.-J. Xu, Morphology control, defect engineering and photoactivity tuning of ZnO crystals by graphene oxide—a unique 2D macromolecular surfactant. *Phys. Chem. Chem. Phys.* **16**, 5589–5599 (2014)
35. X. Xue, L. Liu, Z. Wang, Y. Wu, Room-temperature ferromagnetism in hydrogenated ZnO nanoparticles. *J. Appl. Phys.* **115**, 033902 (2014)
36. S. Ghose, A. Sarkar, S. Chattopadhyay, M. Chakrabarti, D. Das, T. Rakshit, S.K. Ray, D. Jana, Surface defects induced ferromagnetism in mechanically milled nanocrystalline ZnO. *J. Appl. Phys.* **114**, 073516 (2013)
37. R.K. Biroju, N. Tilak, G. Rajender, S. Dhara, P.K. Giri, Catalytic free growth of ZnO nanowires on graphene and graphene oxide and its enhanced photoluminescence and photoresponse. *Nanotechnology* **26**, 145601 (2015)
38. T. Taniguchi, H. Yokoi, M. Nagamine, H. Tateishi, A. Funatsu, K. Hatakeyama, C. Ogata, M. Ichida, H. Ando, M. Koinuma, Y. Matsumoto, Correlated optical and magnetic properties in photo-reduced graphene oxide. *J. Phys. Chem. C* **118**, 28258–28265 (2014)
39. T. Tang, N. Tang, Y. Zheng, X. Wan, Y. Liu, F. Liu, Q. Xu, Y. Du, Robust magnetic moments on the basal plane of the graphene sheets effectively induced by OH groups. *Sci. Rep.* **5**, 8448 (2015)
40. A. Diamantopoulou, S. Glenis, G. Zolnierkiwicz, N. Guskos, V. Likodimos, Magnetism in pristine and chemically reduced graphene oxide. *J. Appl. Phys.* **121**, 043906 (2017)
41. K. Bagani, M.K. Ray, B. Satpati, N. R. Ray, M. Sarder, S. Banerjee, Contrasting magnetic properties of thermally and chemically reduced graphene oxide. *J. Phys. Chem. C* **118**, 13254–13259 (2014)
42. D. Lee, J. Seo, Magnetic frustration of graphite oxide. *Sci. Rep.* **7**, 44690 (2017)
43. J. Chen, W. Zhang, Y. Sun, Y. Zheng, N. Tang, Y. Du, Creation of localized spins in graphene by ring-opening of epoxy derived hydroxyl. *Sci. Rep.* **6**, 26862 (2016)
44. K. Bagani, A. Bhattacharya, J. Kaur, A. Rai Chowdhury, B. Ghosh, M. Sardar, S. Banerjee, Anomalous behavior of magnetic coercivity in graphene oxide and reduced graphene oxide. *J. Appl. Phys.* **115**, 023902 (2014)
45. S. Qin, Q. Xu, Room temperature ferromagnetism in N₂ plasma treated graphene oxide. *J. Alloy. Compd.* **692**, 332–338 (2017)
46. B. Panigrahy, M. Aslam, D.S. Misra, M. Ghosh, D. Bahadur, Defect-related emissions and magnetization properties of ZnO nanorods. *Adv. Funct. Mater.* **20**, 1161–1165 (2010)
47. W. Liu, W. Li, Z. Hu, Z. Tang, X. Tang, Effect of oxygen defects on ferromagnetic of undoped ZnO. *J. Appl. Phys.* **110**, 013901 (2011)
48. P. Zhan, W. Wang, C. Liu, Z. Li, Z. Zhang, P. Zhang, B. Wang, X. Cao, oxygen vacancy-induced ferromagnetism in un-doped ZnO thin films. *J. Appl. Phys.* **111**, 033501 (2012)
49. T. Tietze, P. Audehm, Y.-C. Chen, G. Schtz, B.B. Straumal, S.G. Protasova, A.A. Mazilkin, P.B. Straumal, T. Prokscha, H. Luetkens, Z. Salman, A. Suter, B. Baretzky, K. Fink, W. Wenzel, D. Danilov, E. Goering, Interfacial dominated ferromagnetism in nanograined ZnO: a μ SR and DFT study. *Sci. Rep.* **5**, 8871 (2015)
50. Z. Li, W. Zhong, X. Li, H. Zeng, G. Wang, W. Wang, Z. Yang, Y. Zhang, Strong room-temperature ferromagnetism of ZnO nanostructure arrays via colloidal template. *J. Mater. Chem. C* **1**, 6807–6812 (2013)
51. K. Saravanan, G. Jayalakshmi, S. Chandra, B.K. Panigrahi, R. Krishnan, B. Sundaravel, S. Annapoorani, D.K. Shukla, P. Rajput, D. Kanjilal, The influence of carbon concentration on the electronic structure and magnetic properties of carbon implanted ZnO thin films. *Phys. Chem. Chem. Phys.* **19**, 13316–13323 (2017)
52. X. Battle, A. Labarta, Finite-size effects in fine particles: magnetic and transport properties. *J. Phys. D* **35**, R15–R42 (2002)